Volume 1
Number 1
January 2023
Pages 1–96

EES Catalysis

rsc.li/EESCatalysis

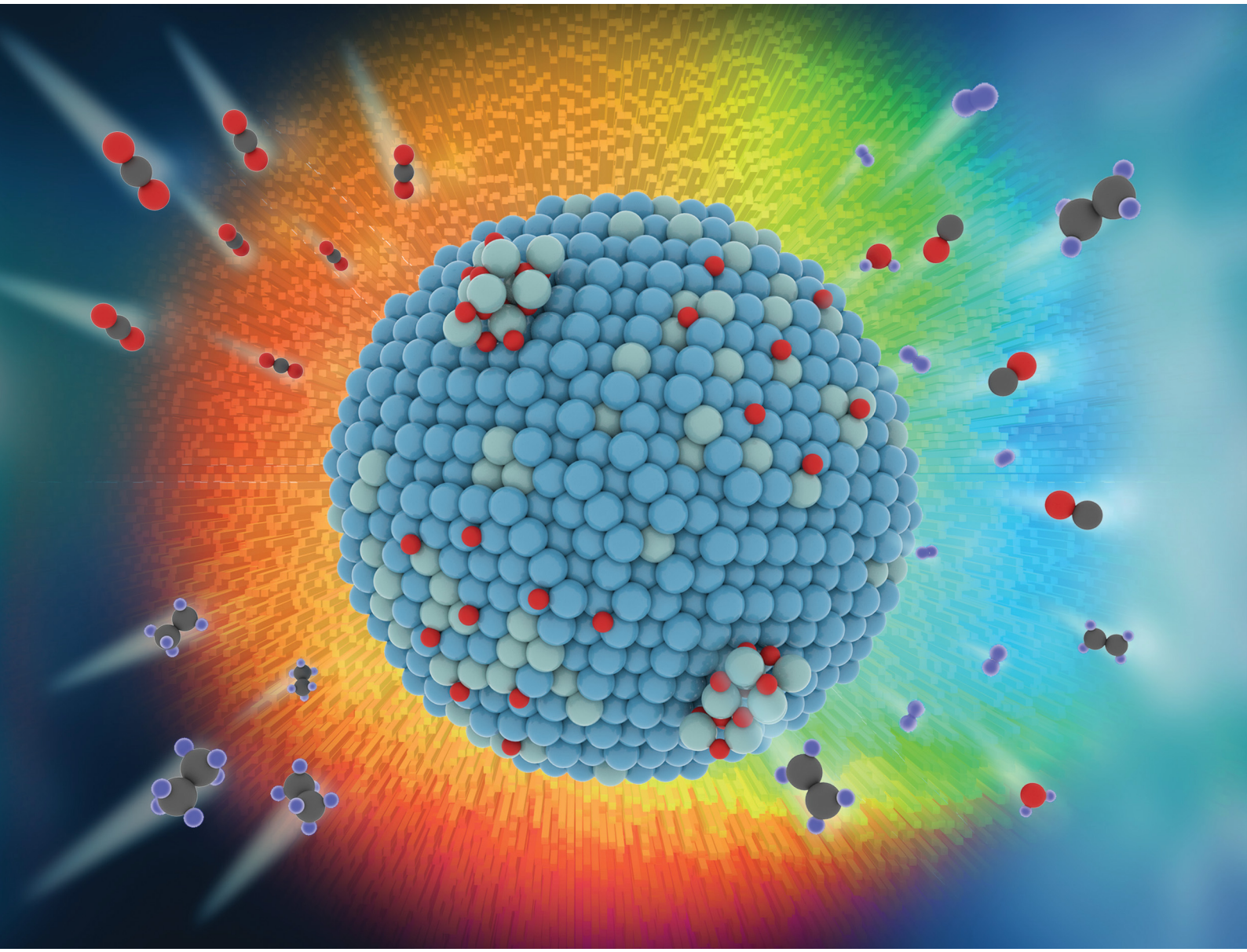

ISSN 2753-801X

ROYAL SOCIETY OF CHEMISTRY

PAPER

Jingguang G. Chen, Ping Liu *et al.*
Descriptor-based identification of bimetallic-derived catalysts for selective activation of ethane with CO_2

EES Catalysis

PAPER

View Article Online
View Journal | View Issue

Cite this: *EES Catal.*, 2023, 1, 17

Descriptor-based identification of bimetallic-derived catalysts for selective activation of ethane with CO_2†

Haoyue Guo, ‡[a] Zhenhua Xie,‡[ab] Xuelong Wang,[a] Jingguang G. Chen *[ab] and Ping Liu *[a]

Received 19th September 2022,
Accepted 15th October 2022

DOI: 10.1039/d2ey00051b

rsc.li/eescatalysis

The selective activation of ethane with CO_2 offers a promising strategy to simultaneously reduce the greenhouse gas and upgrade the underutilized ethane to value-added chemicals. Herein, the catalytic reactions of ethane and CO_2 over a series of indium (In)-based bimetallic-derived catalysts were investigated by combining catalytic evaluation, *in situ* characterization and Density Functional Theory (DFT) calculations. The DFT-calculated energetics along the dry reforming of ethane pathway to produce syngas and oxidative dehydrogenation of ethane to produce ethylene were consistent with the trend in experimentally observed selectivity. Combining the results currently collected for In-based bimetallic catalysts with those previously reported for other bimetallic systems, a descriptor-based model was used to scale the ethylene selectivity over a wide range of bimetallic systems. Furthermore, results from the current study enhanced the mechanistic understanding of the importance that the binding strength of the initial reaction intermediates played in controlling the selective activation of ethane with CO_2.

Broader context

In recent decades, increasing anthropogenic CO_2 emissions and verified huge shale gas reserves have attracted intensive interests in simultaneously upgrading CO_2 and C_2+ light alkanes into different types of important industrial feedstocks (*e.g.*, syngas, olefins, aromatics and oxygenates) at ambient pressure. One of the challenges is how to control the selective scission of C–H/C–C bonds in alkanes. However, the development of selective catalysts, such as those from the bimetallic-derived systems, is hindered by the ambiguous structure–function relationship due to the structural complexity of supported catalysts. The present work is motivated to identify general descriptors not only to predict the thermodynamically favorable bimetallic-derived structures under CO_2-assisted alkane activation conditions, but also to provide mechanistic insights into the selective bond cleavage in alkanes. Herein, ethane–CO_2 reaction over a wide range of bimetallic-derived catalysts was adopted as a case study to unravel the structure–function relationship over two types of representative structures. Two general descriptors, formation energy of alloy surfaces and the corresponding binding energy to oxygen, were utilized to correlate catalytic performance with DFT-calculated values. The identification of these two general descriptors opens new opportunities to the rational design of highly selective catalysts for simultaneously upgrading light alkanes and CO_2.

1. Introduction

The rapid increase of carbon dioxide (CO_2) emissions in the past decades has contributed to the global climate change.[1] To reduce CO_2 emissions, several strategies such as CO_2 capture and catalytic conversion have been proposed.[2–6] One promising route is the utilization of light alkanes to directly activate CO_2 to value-added products, such as syngas, olefins, aromatics and oxygenates.[7–10] The recent shale gas boom has significantly increased the supply of light alkanes, with the fraction of ethane (C_2H_6) being up to 10 vol%.[11] Therefore, the catalytic reactions between CO_2 and C_2H_6 provide a promising strategy to simultaneously reduce the greenhouse gas emissions and upgrade the underutilized C_2H_6 to important industrial chemicals. Depending on the selective bond cleavage of C_2H_6, there are mainly two pathways, *i.e.*, dry reforming of ethane (DRE) to produce syngas ($C_2H_6 + 2CO_2 \rightarrow 4CO + 3H_2$) *via* C–C

[a] *Chemistry Division, Brookhaven National Laboratory, Upton, NY 11973, USA. E-mail: jgchen@columbia.edu, pingliu3@bnl.gov*
[b] *Department of Chemical Engineering, Columbia University, New York, NY 10027, USA*

† Electronic supplementary information (ESI) available: EXAFS spectra of bimetallic-derived catalyst; DFT-optimized structures and corresponding energies for bimetallic surfaces with/without adsorption of reaction intermediates. See DOI: https://doi.org/10.1039/d2ey00051b

‡ Haoyue Guo and Zhenhua Xie contributed equally.

and C–H bond cleavage and oxidative dehydrogenation of ethane (ODHE) to produce ethylene ($C_2H_6 + CO_2 \rightarrow C_2H_4 + CO + H_2O$) *via* selective C–H bond session while protecting the C–C bond.[7–10]

Bimetallic-derived catalysts, either in the metallic or oxidized form, typically feature distinct catalytic properties and are often superior to those of either monometallic component due to the ligand, ensemble and strain effects.[12] A number of bimetallic-derived catalysts have been used for the reactions of C_2H_6 with CO_2, such as Co–Mo,[13] Ni–Mo,[13] Ni–Al,[14,15] Ni–Fe,[13,16,17] Pt–Co,[13] Pt–Ni,[18,19] Pt–Ga,[20] Pt–Ce,[21] Pt–In,[20] Pt–Sn,[22] Pd–Fe,[23] Pd–Co[24] and Pd–In.[24] The enhanced catalytic properties have been proposed to be associated with changes in the compositions and structures.[25–27] For example, Yan *et al.*[16] reported that by changing the ratio of bimetallic components, the active phases under reaction conditions can be transformed, leading to the distinguished reaction pathways: Ni_3Fe prefers to stay as mixed alloy during the activation of C_2H_6 by CO_2 and is more favorable for C–C bond scission; while $NiFe_3$ prefers to form the Ni/FeO_x interface, which is the active site for C–H bond scission. Recently, Xie *et al.* revealed that the reaction-induced surface phase transformation can tune the selectivity in the scission of the C–C and C–H bonds of C_2H_6 on $PdCo_x/CeO_2$ and $PdIn_x/CeO_2$ catalysts, respectively.[24] Based on the case studies of a series of Pd-based bimetallic catalysts, the interplay of two descriptors was proposed:[24] the formation energy of the alloy surface and the reactive oxygen binding energy, which scaled well with the C_2H_4 selectivity. However, it remains unclear whether the previously identified descriptors can be employed universally to capture the CO_2-assisted C_2H_6 activation beyond the Pd-based catalysts.

Herein, the selective activation of C_2H_6 with CO_2 was studied over a series of In-based bimetallic catalysts. The C_2H_4 selectivity was investigated using experimental studies of synthesis, catalytic testing and *in situ* characterization, followed by DFT calculations to gain better mechanistic understanding, validate the descriptors previously identified for Pd-based bimetallic catalysts and eventually use them as universal descriptors for identifying promising bimetallic-derived catalysts. The selection of In-based bimetallic catalysts was primarily inspired by their intriguing performance for CO_2-assisted propane dehydrogenation, where the catalytic activity was attributed to the In redox activity (In^0 and In^{III}) and the associated transfer of chemisorbed oxygen (*O).[28–31] Moreover, previously the change in the ratio of Pt : In in bimetallic Pt–In derived catalysts was also found to influence the active phases and therefore the performance during the direct dehydrogenation of C_2H_6.[20]

The present experimental and DFT studies of In-based catalysts provided insights into controlling the DRE and ODHE pathways to produce syngas and C_2H_4, respectively. The combination of results of In-based systems from current study with those of other bimetallic-derived catalysts reported previously, a descriptor-based prediction of selectivity was achieved for the simultaneous upgrading of C_2H_6 and CO_2 over a wide range of bimetallic catalysts. It not only facilitates the discovery of new catalysts, but also promotes the mechanistic understanding of selectivity-tuning introduced by forming different bimetallic-derived structures. Furthermore, a volcano relationship was observed between the binding difference of $*CH_3CH_2O$ and $*CH_3CH_2$ intermediates and the corresponding C_2H_4 selectivity over diverse bimetallic systems.

2. Methods

2.1. Experimental methods

All In-based bimetallic catalysts were synthesized using a slurry method. For each synthesis, desired amounts of metal precursors [$Rh(NO_3)_3{\cdot}2H_2O$, $Pt(NH_3)_4(NO_3)_2$, $Co(NO_3)_2{\cdot}6H_2O$, $Ni(NO_3)_2{\cdot}6H_2O$, or $Cu(NO_3)_2{\cdot}3H_2O$] were simultaneously dissolved with $In(NO_3)_3{\cdot}xH_2O$ in 30 ml of DI water to achieve a M/In atomic ratio of 1 : 3 at room temperature. Afterwards, the solution was ultrasonicated for 15 min before adding the CeO_2 support, followed by another ultrasonication of 30 min. The slurry suspension was continuously stirred and dried at 343 K overnight, after which the dried sample was calcined in static air at 673 K for 4 h with a heating rate of 1.0 K min^{-1}. More details about the loading amounts of each metal elements can be found in the ESI.†

All the catalysts were evaluated using a flow reactor (quartz tube, 4 mm ID, 6.35 mm OD) at ambient pressure. For each test, unless specified, approximately 100 mg of catalyst (60–80 mesh) was loaded into the isothermal zone of the quartz tube and fixed by two pieces of quartz wool on both ends. The catalyst was reduced in 50 vol% H_2 in Ar (total 40 ml min^{-1}) at 723 K for 1 h and then heated to 873 K under Ar (40 ml min^{-1}) in 15 min. The catalyst was subsequently exposed to C_2H_6/CO_2/Ar (10/10/20 ml min^{-1}) at 873 K for catalytic evaluation for 12 h. The gas line from the reactor outlet to the gas chromatography (GC) inlet was wrapped by heating tapes and maintained at 423 K to avoid any condensation of water vapor. The product stream was analyzed by an Agilent 7890B GC (PLOT Q and MOLESEIVE columns) equipped with a thermal conductivity detector (TCD) and a flame ionized detector (FID). The elemental (C, H, O) balances were within 100 ± 2% for all the experiments. Procedures for calculating conversion (X), C_2H_6-based selectivity (S) and yield (Y) were the same to those described in a previous study.[24]

The *in situ* X-ray absorption fine structure (XAFS) spectra of the Pt L_3-edge, Rh K-edge and In K-edge were collected at Beamline 7-BM (QAS) of the National Synchrotron Light Source II (NSLS-II) at Brookhaven National Laboratory, following the same experimental methods described in a previous study.[24] XAFS spectra were continuously collected *in situ* under Helium at 298 K, 50 vol% H_2 at 723 K, He purging at 823 K, and the reaction stream of CO_2 and C_2H_6 at 823 K. Rh, Pt and In foils were used as standard references for energy calibrations as well as to obtain the passive electron reduction factor (S_0^2) used for the fitting of the extended X-ray absorption fine structure (EXAFS) spectra. The EXAFS fittings were performed with the scattering information (amplitude and phase functions) extracted from the model compounds (see more details in Fig. S1 and S2 in ESI†). Metal oxide references (Rh_2O_3, PtO_2,

and In_2O_3) were also measured for identifying oxidation states using the X-ray absorption near edge structure (XANES) results. Data processing was performed using the IFEFFIT package.

2.2. DFT calculations

Spin-polarized DFT calculations were performed with the projector-augmented-wave (PAW) approach[32,33] and the generalized gradient approximation (GGA) exchange–correlation functional by Perdew, Burke and Ernzerhof (PBE)[34] as implemented in the Vienna Ab Initio Simulation Package (VASP).[32,35] A kinetic energy cutoff for the plane wave basis of 400 eV was employed. The Methfessel–Paxton order I method was used to describe the Fermi-distribution of electronic states in the metallic systems with an artificial electronic temperature of $k_BT = 0.2$ eV. The total energy was converged better than 10^{-7} eV per atom, and the final force on each atom was less than 0.03 eV $Å^{-1}$. To calculate the descriptors for the CO_2-assisted activation of ethane, a 4-layer 2 × 2 surface slab was constructed to describe the (111) surface phases of AB_3 bimetallic alloys, where the first Brillouin zone was sampled on a Γ-centered 3 × 3 × 1 k-mesh. Following our previous study,[24] three surface models were considered for bare AB_3(111): the bulk-terminated surface to simulate the stoichiometric structure AB_3(111), the skin A/B(111) or the sandwich B/A/B(111) models to describe the two extreme cases of surface segregation. In addition, the configurations under activation of ethane with CO_2, where chemisorbed oxygen (*O) was likely formed *via* CO_2 dissociation,[23] were also considered by the saturate adsorption of a layer of *O on top of the three types of alloy surfaces and formation of oxide–metal interfaces.

To describe the potential energy diagram on the selected bimetallic-derived interfaces, InO_x/Rh(111) and InO_x/Pt(111) were modeled by placing a small InO_x cluster on a 4-layer 5 × 5 Rh(111) and Pt(111) surfaces, respectively. The choice of such small cluster was a compromise between the computational cost and reasonable size to account for the characterized nanoparticles experimentally. The formation energies of the InO_x cluster on the metal surfaces were calculated with reference to the corresponding metal surface, metallic In and gaseous oxygen. The variation in formation energy with the increasing ratio of O : In, x, was calculated for InO_x/Pt(111) or InO_x/Rh(111) and the surface with the lowest formation energy was selected for further catalytic studies.

A 20 Å thick vacuum was added along the direction perpendicular to the surface to avoid the interactions between the slabs. During geometry optimization, the bottom two layers were fixed at the bulk positions while the remaining layers were allowed to relax, and dipole corrections were included in the calculations. The formation energies of alloy surfaces and the reactive oxygen binding energies were calculated following the previous study.[24] Wherein, the formation energies of alloy surfaces were calculated referenced to each metal surface. The reactive oxygen binding energies were determined by referring to the most stable alloy surface and gaseous oxygen, accounting for possible phase transitions. The binding energy of an adsorbate is calculated as $E_b = E_{adsorbate/slab} - E_{slab} - E_{adsorbate}$, where $E_{adsorbate/slab}$, E_{slab} and $E_{adsorbate}$ are the DFT-calculated total energies of slab with the adsorbate, bare slab and the adsorbate species in the gas phase, respectively.

3. Results and discussion

3.1. Experimental evaluation of activity and selectivity

Several CeO_2-supported AIn_3 (A = Co, Ni, Cu, Rh, Pd, Pt) were synthesized, characterized, and tested for the CO_2-assisted activation of C_2H_6. As shown in Fig. 1a, all the In-based catalysts exhibited stable conversion of CO_2 and C_2H_6 after the initial 2 h. Among the catalysts investigated in the current study, $RhIn_3$/CeO_2 showed the highest conversion (20.0%) of CO_2 at the steady state, followed by $PtIn_3$/CeO_2 (11.0%), $NiIn_3$/CeO_2 (6.3%),

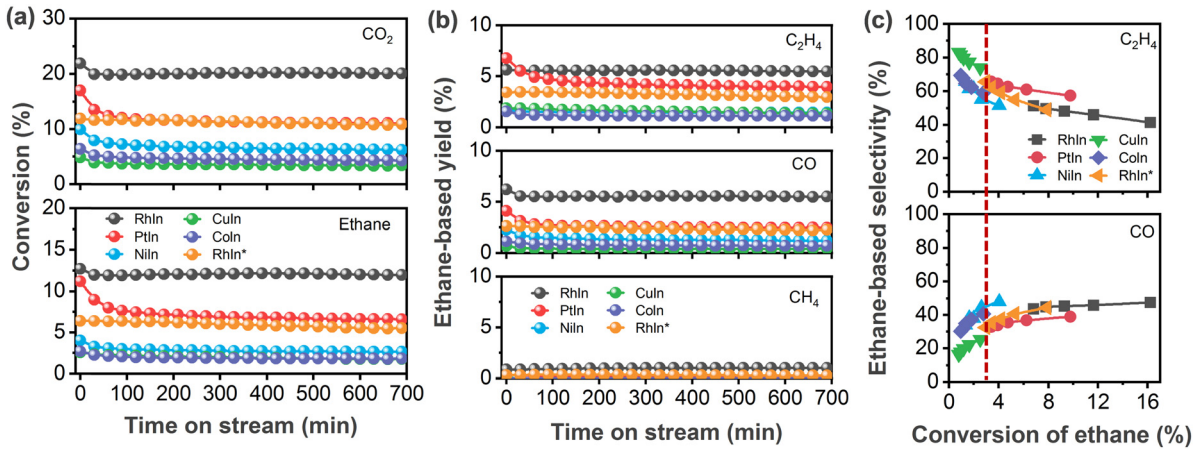

Fig. 1 Catalytic performance of In-based bimetallic catalysts for the CO_2–ethane reaction. (a) Conversion of CO_2 and ethane as a function of time on stream; (b) ethane-based yield of ethylene, CO and methane along with time on stream; (c) ethane-based selectivity of ethylene and CO at different conversion of ethane. Reaction conditions: (a and b) 100 mg of catalyst, 1 atm, 873 K, $C_2H_6/CO_2/Ar$ = 10/10/20 ml min^{-1}; (c) 100 mg of catalyst, 1 atm, 873 K, $C_2H_6/CO_2/Ar$ = 5/5/10, 10/10/20, 15/15/30, 20/20/40, 25/25/50 ml min^{-1}. Notes: the catalyst loading for RhIn* was 40 mg; the ethane-based yield or selectivity of ethylene and CO means that such products were ethane-derived species.

Table 1 Summary of catalytic performance over different MIn_3/CeO_2 catalysts for the CO_2–ethane reaction at 873 K with comparable ethane conversion

	Conversion (%)	Selectivity (%)		
Catalysts	C_2H_6	CH_4	CO	C_2H_4
$PtIn_3/CeO_2$[a]	3.4	1.4	33.0	65.6
$NiIn_3/CeO_2$[b]	2.6	0.2	44.5	55.3
$CuIn_3/CeO_2$[c]	2.5	0.6	25.5	73.9
$CoIn_3/CeO_2$[d]	2.8	0.4	40.6	59.0
$RhIn_3/CeO_2$[e]	2.9	1.9	32.5	65.6
$PdIn_3/CeO_2$[fg]	3.1	0.0	11.0	89.0

Notes: unless denoted, the catalysts were evaluated with the reaction conditions of 1 atm, 100 mg of catalyst, 873 K. [a] $C_2H_6/CO_2/Ar$ = 25/25/50 ml min^{-1}. [b] $C_2H_6/CO_2/Ar$ = 10/10/20 ml min^{-1}. [c] $C_2H_6/CO_2/Ar$ = 5/5/10 ml min^{-1}. [d] $C_2H_6/CO_2/Ar$ = 5/5/10 ml min^{-1}. [e] 40 mg of catalyst, $C_2H_6/CO_2/Ar$ = 25/25/50 ml min^{-1}. [f] $C_2H_6/CO_2/Ar$ = 10/10/20 ml min^{-1}. [g] The data were collected from ref. 24.

$PdIn_3/CeO_2$ (4.5%),[24] $CoIn_3/CeO_2$ (4.3%), and $CuIn_3/CeO_2$ (3.4%) in a decreasing sequence. Likewise, the C_2H_6 conversion followed a similar trend: $RhIn_3/CeO_2$ (12.0%) > $PtIn_3/CeO_2$ (6.6%) > $PdIn_3/CeO_2$ (3.1%)[24] ≈ $NiIn_3/CeO_2$ (2.7%) > $CoIn_3/CeO_2$ (1.8%) ≈ $CuIn_3/CeO_2$ (1.8%). Fig. 1b showed that the main products were C_2H_4 and CO as well as a minor amount of methane (CH_4). $RhIn_3/CeO_2$ (5.5%) and $PtIn_3/CeO_2$ (4.0%) exhibited higher yields of C_2H_4 than the previously reported $PdIn_3/CeO_2$ catalyst (2.8%) as well as the other MIn_3/CeO_2 (M = Ni, Co and Cu) catalysts (1.1–1.4%). The highest and lowest CO yields were observed over $RhIn_3/CeO_2$ (5.5%) and $PdIn_3/CeO_2$ (0.3%), respectively. Given the different conversions among different catalysts, for the sake of properly comparing selectivity, the C_2H_6 conversion was varied by changing the space velocity at the same reaction temperature (873 K) to obtain comparable values (around 3% conversion, denoted by the dashed line in Fig. 1c). As summarized in Table 1, the C_2H_4 selectivity followed the trend of $PdIn_3/CeO_2$ (89.0%) > $CuIn_3/CeO_2$ (73.9%) > $RhIn_3/CeO_2$ (65.6%) ≈ $PtIn_3/CeO_2$ (65.6%) > $CoIn_3/CeO_2$ (59.0%) > $NiIn_3/CeO_2$ (55.3%) in a decreasing sequence, while it followed the reverse trend for the C_2H_6-based CO selectivity.

3.2. Characterization using *in situ* XAFS

Because $RhIn_3/CeO_2$ and $PtIn_3/CeO_2$ showed the highest activity for CO_2 and C_2H_6 conversions, the chemical states of these two catalysts under different conditions were characterized using *in situ* XAFS measurements. According to the Rh K-edge XANES results (Fig. 2a), Rh in the fresh sample retained a chemical state resembling Rh^{3+} in Rh_2O_3, which was reduced at 723 K under the hydrogen atmosphere as indicated by the diminished white line and a shift to lower energy. It should be noted that the XANES feature was much different from that of Rh foil, suggesting the formation of Rh–In bonds where the orbitals rehybridized. Meanwhile, the In K-edge XANES features (Fig. 2b) indicated that In was reduced to a state between In^0 and In^{3+}, likely due to the co-presence of InO_x oxides and metallic (or Rh_xIn_y) species. Upon exposure to the reaction stream (C_2H_6 and CO_2) at 823 K, both the XANES features of Rh and In K-edges remained nearly unchanged, suggesting the robust feature of the above structures. Likewise, as shown in Fig. 2c and d, after reduction at 723 K the Pt L_3-edge and In K-edge XANES results of $PtIn_3/CeO_2$ also revealed that a metallic character of Pt, but different from that of Pt foil, while In was in a mixed state with both oxidic and metallic features, again suggesting the co-presence of the InO_x and PtIn alloy structures, which remained unchanged in the presence of C_2H_6 and CO_2 at 823 K. Overall, the XANES results indicated the presence of both InO_x and RhIn (or PtIn) under reaction conditions, consistent with the corresponding EXAFS results (Fig. S1, S2 and Table S1, ESI†) that revealed the presence of both In–O and In–Rh (or In–Pt) coordination.

3.3. Mechanistic understanding using DFT calculations

DFT calculations were performed on the highly active In-based catalysts observed experimentally (Fig. 1), $RhIn_3$ and $PtIn_3$, to gain a mechanistic understanding of the activation of C_2H_6 with CO_2. Wherein, the CeO_2 support for the bimetallic catalysts was found experimentally to play similar roles, *i.e.* facilitating the CO_2 dissociation and providing reactive oxygen species, *O, during the reaction.[13,16,18,23,24] Thus, as shown previously, it is reasonable to compare the theoretical predictions based on unsupported bimetallic AB_3 model surfaces with the experimentally measured trends on supported AB_3/CeO_2 catalysts.[13,16,18,23,24]

The stable surface structures of $RhIn_3$ and $PtIn_3$ under reaction condition were firstly determined using DFT calculations (Fig. S3, ESI†). The results showed the preference to the inverse model with InO_x oxide supported on the Rh(111) (Fig. S4, ESI†) and Pt(111) (Fig. S5, ESI†) surfaces due to the strong interaction between *O, likely produced from CO_2 dissociation, and the surface In atoms, while the subsurface remained as the bimetallic. This is consistent with the *in situ* XAFS results showing the mixture of In in both oxidative and metallic states (Fig. 2 and Fig. S1, S2, ESI†). For the inverse model, a small InO_x cluster containing two In atoms was chosen as a compromise of computational cost and reasonable size to depict the InO_x nanostructures formed on the metal surface under the reaction conditions. The effect of In : O ratio on the relative cluster stability was evaluated based on the formation energies (Fig. S4 and S5, ESI†). On Rh(111) (Fig. S4, ESI†), the most stable configuration is In_2O_5/Rh(111) with the additional *O locating at the interfacial fcc hollow site of Rh(111), rather than that on In_2O_5 cluster. In comparison, the interaction of the InO_x cluster on Pt(111) (Fig. S5, ESI†) is much weaker and In_2O_7/Pt(111) is preferred. Yet, the additional *O still favors the interfacial fcc hollow site of Pt(111).

The DRE (C–C bond scission), and the ODHE (C–H bond scission) reaction pathways were calculated to describe the observed variation in C_2H_4 selectivity from the CO_2–ethane reaction over the stable surfaces under reaction conditions (Fig. 3). We note here that only the reaction energies for the elementary steps involved were calculated, by assuming a BEP-like correlation between the reaction energy and the corresponding activation barrier according to our previous DFT studies on the activation of light alkanes with CO_2.[24,36] On

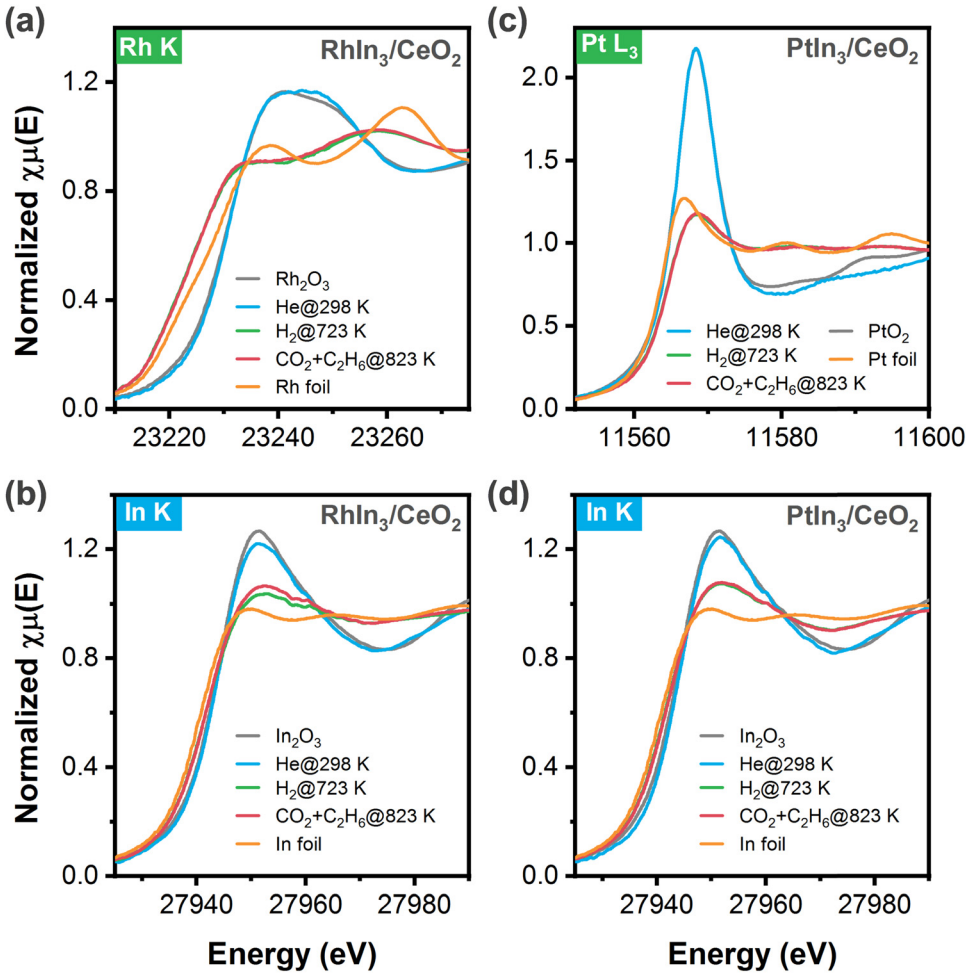

Fig. 2 *In situ* XANES spectra of $RhIn_3/CeO_2$ and $PtIn_3/CeO_2$ catalysts as well as reference samples: (a and b) referred to the *in situ* XANES spectra of Rh and In K-edges, respectively, of $RhIn_3/CeO_2$ under different conditions; (c and d) referred to the *in situ* XANES spectra of Pt L_3-edge and In K-edge, respectively, of $PtIn_3/CeO_2$ under different conditions. Note: standard referential samples (metal foils: Rh, Pt, and In; metal oxides: Rh_2O_3, PtO_2, and In_2O_3) were also measured for comparison in XANES.

In_2O_5/Rh(111), with the presence of *O at the interfacial fcc hollow site of Rh and in a binding energy of −1.72 eV (Fig. 3 and Fig. S6 and Table S2, ESI†), the initial dissociative adsorption of C_2H_6 to produce $*CH_3CH_2$ along the ODHE pathway is slightly more favorable (ΔE = 0.52 eV) than the formation of $*CH_3CH_2O$ along the DRE pathway (ΔE = 0.76 eV, Fig. 3). The further dehydrogenation of $*CH_3CH_2$ to $*CH_2CH_2$ along the ODHE pathway is exothermic (ΔE = −0.39 eV), and the most endothermic process is the desorption of $*CH_2CH_2$ (ΔE = 0.82 eV), which is likely overcome under the reaction temperature at 823 K. It is noticed that the elementary steps involved in the DRE pathway show a different energy profile from that along the ODHE pathway (Fig. 3). Once $*CH_3CH_2O$ is formed, not only its further dehydrogenations to $*CH_3CHO$ (ΔE = 0.31 eV) and $*CH_3CO$ (ΔE = −0.50 eV), but also the following C–C bond cleavage to produce *CO (ΔE = −0.26 eV) are facile (Fig. 3). Overall, the DFT results suggest that, although the initial reaction step on In_2O_5/Rh(111) favors the ODHE leading to the C_2H_4 production, the DRE resulting in syngas production is also feasible due to the facile subsequent steps after the initial formation of $*CH_3CH_2O$, which reasonably agrees with the experimentally measured intermediate C_2H_4 selectivity of 65.6%.

Compared to In_2O_5/Rh(111), with the lower In : O ratio In_2O_7/Pt(111) enables the significant bond weakening for *O located at the interfacial fcc hollow site of Pt(111) (Fig. S7, ESI†), going from −1.72 eV to −0.86 eV in binding energy (Table S2, ESI†). While the preference to form $*CH_3CH_2$ (ΔE = −0.11 eV) along the ODHE pathway over $*CH_3CH_2O$ (ΔE = 1.04 eV) along the DRE pathway is greatly increased. In considering the energetics for the initial C_2H_6 dissociative adsorption, the preference of ODHE over DRE is more significant (−0.11 eV *vs.* 1.04 eV) for In_2O_7/Pt(111) than that of In_2O_5/Rh(111) (0.52 eV *vs.* 0.76 eV), and thus, a higher C_2H_4 selectivity on In_2O_7/Pt(111) should be expected (Fig. 3). However, the $*CH_2CH_2$ desorption along the ODHE pathway is more facile on In_2O_5/Rh(111) than In_2O_7/Pt(111) (0.82 eV *vs.* 1.08 eV), and therefore a lower C_2H_4 selectivity on In_2O_7/Pt(111) is likely observed. The interplay of the two factors operating in an opposite direction likely contributes to a similar C_2H_4 selectivity for the two catalysts as observed experimentally.

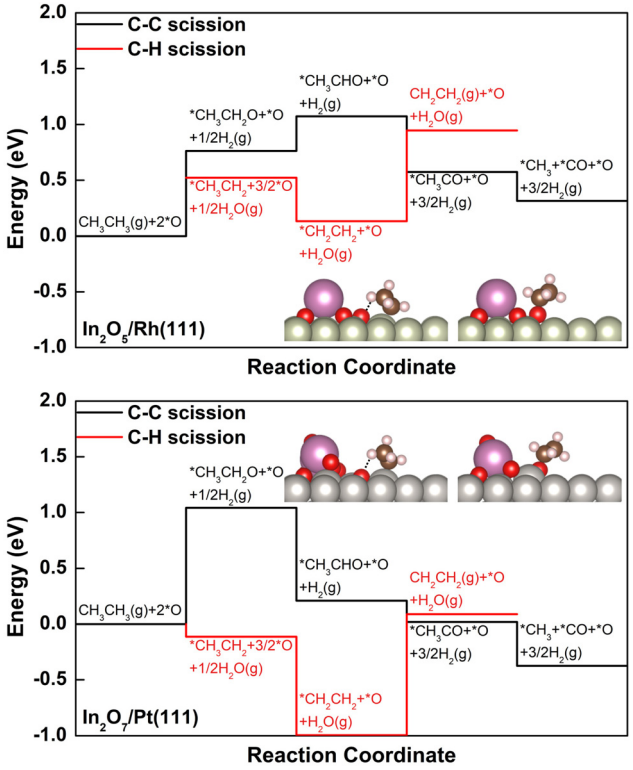

Fig. 3 Potential energy diagrams for dry reforming reaction of ethane (DRE or C–C bond scission) and oxidative dehydrogenation reaction of ethane (ODHE or C–H bond scission) on In_2O_5/Rh(111) (top) and In_2O_7/Pt(111) (bottom). The DFT-optimized structures of selected key intermediates *CH_3CH_2 + *O (left) and *CH_3CH_2O (right) were included as insets and the hydrogen bonds were shown by dotted lines (In: pink; Pt: gray; Rh: ivory; O: red; C: brown; H: white).

3.4. Identifying selective bimetallic-derived catalysts using descriptors

Our previous study of 14 Pd-based bimetallic catalysts[24] identified a contour plot, which described well the relationship between the two identified descriptors (formation energies of alloy surfaces and the reactive oxygen binding energies) and experimentally measured C_2H_4 selectivity. The current study showed that in general such contour plot can be expanded to describe the In-based systems, confirming the universality of the descriptor-selectivity relationship identified previously (Fig. 4). That is, depending on the value of calculated descriptors, the bimetallic-derived surfaces can be classified into three major regions: (i) blue region where the bimetallic systems prefer to segregate before reaction due to the high alloy surface formation energy (>-0.5 eV), while under the reaction the reactive oxygen binding energy is too weak (>-2 eV) to form metal oxides, leading to low C_2H_4 selectivity; (ii) red region where the metal/oxide interfaces during the reaction are preferentially formed by featuring strong oxygen binding and low alloy surface formation energy, yielding high C_2H_4 selectivity; (iii) green region where the mixed alloys with the bulk-terminated configuration are favored despite the interaction with the reactive environment, and the transition to metal/oxide interface is hindered by either the

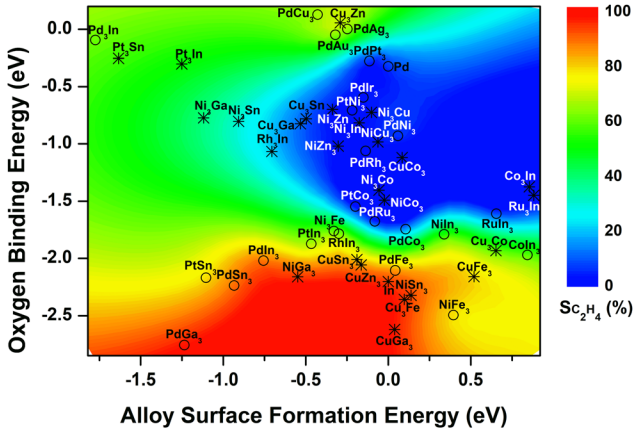

Fig. 4 Descriptor-based contour map (circles: bimetallic systems where C_2H_4 selectivity have been measured experimentally; asterisks: bimetallic systems that have not been explored yet). The selectivity of Pd-based catalysts was cited from ref. 24.

oxygen binding not being strong enough or the alloy surface formation not being favorable enough, featuring intermediate C_2H_4 selectivity. Besides, the addition of the results for In-based bimetallic catalysts also enhances the predictive capability, which features the expansion to describe the systems with more negative (<-1.25 eV) or positive (>0.25 eV) alloy surface formation energy (Fig. 4).

Based on the color-coded contour plot (Fig. 4), one can roughly estimate the corresponding C_2H_4 selectivity from CO_2-activation of C_2H_6 over a bimetallic system, simply using the DFT-calculated values for the two descriptors, reactive oxygen binding energy and alloy surface formation energy. Accordingly, the C_2H_4 selectivity measured previously for bimetallic-derived systems, such as $NiFe_3$ (experiment: 78%[16] *vs.* descriptor-based estimation: ~75%), $PdFe_3$ (86%[23] *vs.* ~85%), $PtCo_3$ (1%[13] *vs.* ~0%), $PtNi_3$ (1%[18,19] *vs.* ~0%), and $PtSn_3$ (83%[36] *vs.* ~75%) can be estimated, which reproduced the experimental values reasonably well. Therefore, the DFT-calculated formation energies of alloy surfaces and the reactive oxygen binding energies can be used as universal descriptors to screen the bimetallic-derived catalysts for the selective activation of C_2H_6 with CO_2.

In addition, the two descriptors were also calculated for other bimetallic catalysts based on the stable surface structures (Fig. S3, ESI†), which have not been studied previously, aiming to predict the C_2H_4 selectivity during activation of C_2H_6 with CO_2 based on the contour plot in Fig. 4. One group involved the In-based bimetallic alloys, including $RuIn_3$ and series of M_3In (M = Pd, Pt, Rh, Cu, Ni, Co, Ru) (asterisk, Fig. 4). However, none of these candidates falls into the red region with the possible high C_2H_4 selectivity. The other group considered the earth abundant elements, Ni-based (MNi_3 and M_3Ni, M = Cu, Ni, Co, Zn, Ga, Sn, Fe) and Cu-based (MCu_3 and M_3Cu) bimetallic catalysts (asterisk, Fig. 4). Among the 20 Ni- and Cu-based systems, $NiGa_3$, $NiSn_3$, $CuGa_3$, $CuSn_3$, $CuZn_3$ and Cu_3Fe prefer to form the metal/oxide interfaces and fall into the red region featuring strong binding to oxygen and thus a high C_2H_4

selectivity is expected. Some other catalysts likely maintain the bulk-terminated mixed alloy surface during the reaction, *i.e.* Ni_3Fe, Ni_3Ga, Ni_3Sn, Cu_3Co and Cu_3Zn, and are featured with either relatively high oxygen binding energy or high surface formation energy in the green region, which should possess a moderate C_2H_4 selectivity and can be potential catalysts for the tandem reactions, *e.g.*, hydroformylation[17,37] and aromatization.[38–40] The remaining bimetallic systems are located in the blue region. Due to both high oxygen binding energy and high alloy surface formation energy, these systems likely segregate, favoring the DRE pathway and thus a low C_2H_4 selectivity.

The descriptor-based scaling (Fig. 4) not only allows the effective prediction of C_2H_4 selectivity during C_2H_6 activation with CO_2 over a large range of bimetallic catalysts, but also provides a database to gain general mechanistic understanding and thus extraction of design principle, which requires the well-dispersion in C_2H_4 selectivity values for potential data mining. Indeed, a group of In or Pd-based bimetallic catalysts was selected from the systems with the predicted C_2H_4 selectivity using DFT-calculated descriptors, making sure the diversity and dispersion over a large range of selectivity. As a result, the difference in binding energy of initial reaction intermediates, $*CH_3CH_2O$ for the DRE pathway and $*CH_3CH_2$ for the ODHE pathway, was found to scale well with the C_2H_4 selectivity during C_2H_6 activation with CO_2. Specifically, a relationship between the binding difference and the C_2H_4 selectivity was observed (Fig. 5), which remained valid by including more systems with reported C_2H_4 selectivity previously, *i.e.*, Fe_3O_7/Ni(111) (Fig. S8, ESI†) as a model to describe $NiFe_3$[16] and Fe_3O_6/Pd(111) (Fig. S9, ESI†) to describe $PdFe_3$.[23] With the binding difference decreasing *via* weakening $*CH_3CH_2O$ and/or strengthening $*CH_3CH_2$ interaction with the surfaces, the ODHE pathway becomes more favorable over the DRE pathway, and thus the C_2H_4 selectivity increases in a sequence: Ni_3In < Pd_3Co < $PdIn_3$ or In_2O_5/Pd(111) < $PdGa_3$ or Ga_2O_5/Pd(111) (the solid line region in Fig. 5). $PdGa_3$ before the reaction or Ga_2O_5/Pd(111) under the reaction is able to balance the binding difference well at the metal–oxide interface (Fig. S10, ESI†), which shows the highest C_2H_4 selectivity among the catalysts investigated. On the other hand, if the strengthening in $*CH_3CH_2$ binding is too strong, it can lower the C_2H_4 selectivity. For example, in the case of In_2O_7/Pt(111), the highly stabilized $*CH_3CH_2$ and $*CH_2CH_2$ hinder the desorption of the product and reduce the C_2H_4 selectivity. However, in order to determine whether a volcano-type relationship exists, more bimetallic-derived catalysts need to be studied, especially those with binding energy difference of $*CH_3CH_2O$ and $*CH_3CH_2$ between that of Ga_2O_5/Pd and In_2O_7/Pt (the dashed line region in Fig. 5). In addition, depending on the nature of active sites the key intermediates responsible for the C_2H_4 selectivity may not necessarily be $*CH_3CH_2O$ and $*CH_3CH_2$, which seem to scale well with the C_2H_4 selectivity for the bimetallic systems studied in Fig. 5. Further studies of a wide range of bimetallic catalysts should be carried out for verification.

In general, for bimetallic alloys that maintain the bulk-terminated alloy surface during the activation of C_2H_6 with CO_2, a low C_2H_4 selectivity is expected. While for those that prefer the phase transformation to metal/oxide interfaces, a higher C_2H_4 selectivity is likely achieved (Fig. 5). The preferential formation of oxide/metal interfaces weakens the binding of *O at the interface where the metal sites are partially oxidized upon interaction with oxides. It also leads to a destabilization for the adsorbed oxygenate ($*C_2H_xO$) species and thus the hindered DRE pathway leading to syngas production. While the presence of *O at the interface enhances the binding of hydrocarbon ($*C_2H_x$) intermediates *via* the formation of hydrogen bonds (Fig. 3), giving rise to the C_2H_4 selectivity by facilitating the ODHE pathway. To achieve a high C_2H_4 selectivity, bimetallic-derived catalysts offer opportunities to tune the reaction pathways. With an appropriate bimetallic combination, the catalyst can bind *O strongly enough to overcome the formation energy of alloy and transform the metallic surface to oxide/metal interfaces under reaction conditions, enabling the selective tuning of $*C_2H_x$ binding more strongly than $*C_2H_xO$, but still moderate enough to allow facile desorption of C_2H_4 from the bimetallic-derived surfaces.

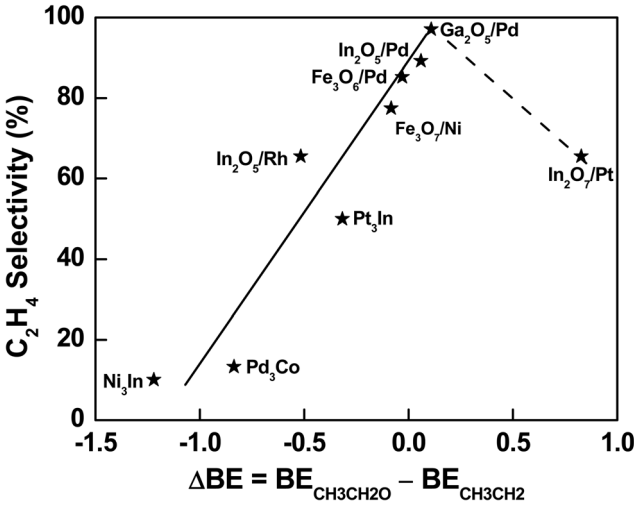

Fig. 5 Correlation between C_2H_4 selectivity and binding energy difference of $*CH_3CH_2O$ and $*CH_3CH_2$, which is the initial intermediate for DRE or C–C bond scission and ODHE or C–H bond scission, respectively. The labels correspond to the most stable structures according to DFT calculations. Note: the selectivity associated with different structures in Fig. 5 was predicted from the descriptor-based contour plot in Fig. 4, which was established based on experimentally measured selectivity reported in Table 1 and our previous studies under similar conditions.[16,23,24]

4. Conclusions

The selective CO_2-assisted activation of ethane was investigated on a series of In-based bimetallic-derived catalysts by combining experimental synthesis, catalytic test, *in situ* characterization and DFT calculations. The mechanistic study on In-based catalysts provided insights into the origin of the observed C_2H_4 selectivity. A scaling relationship was established based on the results for In-based bimetallic catalysts from the current work and others from previous studies, being able to well predict the

C_2H_4 selectivity based on the descriptors (DFT-calculated formation energies of alloy surfaces and the reactive oxygen binding energies) for a wide range of bimetallic systems. Furthermore, our study also opens the opportunity to extract the design principles of bimetallic catalysts for the activation of ethane with CO_2, indicating that the selectivity of bimetallic-derived catalysts between the ODHE and DRE pathways or C_2H_4 and syngas production can be tuned by the relative binding strength of the initial reaction intermediates. Bimetallic-derived catalysts with high C_2H_4 selectivity should bind oxygen strongly to enable the formation of oxide/metal interfaces under reaction conditions, which favor ODHE rather than DRE by binding the $*C_2H_x$ species more strongly than $*C_2H_xO$, but moderately to allow facile removal of $*C_2H_4$.

Conflicts of interest

The authors declare no competing financial interest.

Acknowledgements

This work was financially supported by the Division of Chemical Sciences, Geosciences, & Biosciences, Office of Basic Energy Sciences and carried out at Brookhaven National Laboratory (BNL), operated under contract DE-SC0012704 with the US Department of Energy. The DFT calculations were performed using computational resources at the Center for Functional Nanomaterials, a user facility at BNL supported by the U.S. DOE under Contract No. DE-SC0012704, and at the National Energy Research Scientific Computing Center (NERSC), a U.S. DOE Office of Science User Facility located at Lawrence Berkeley National Laboratory (LBNL), supported by the Office of Science of the U.S. DOE under Contract No. DE-AC02-05CH11231. This work used resources at the 7-BM (QAS) beamline of the National Synchrotron Light Source-II at BNL and was supported in part by the Synchrotron Catalysis Consortium under U.S. Department of Energy, Office of Basis Energy Sciences (Grant No. DE-SC0012704 and DE-SC0012653). Authors also thank Dr Erwei Huang for help with formatting.

References

1 J. Rogelj, P. M. Forster, E. Kriegler, C. J. Smith and R. Séférian, *Nature*, 2019, **571**, 335–342.
2 X. Zhang, S. Han, B. Zhu, G. Zhang, X. Li, Y. Gao, Z. Wu, B. Yang, Y. Liu, W. Baaziz, O. Ersen, M. Gu, J. T. Miller and W. Liu, *Nat. Catal.*, 2020, **3**, 411–417.
3 Y. Nian, Y. Wang, A. N. Biswas, X. Chen, Y. Han and J. G. Chen, *Chem. Eng. J.*, 2021, **426**, 130781.
4 Q. Chang, J. H. Lee, Y. Liu, Z. Xie, S. Hwang, N. S. Marinkovic, A.-H. A. Park, S. Kattel and J. G. Chen, *JACS Au*, 2022, **2**, 214–222.
5 X. Wang, P. J. Ramírez, W. Liao, J. A. Rodriguez and P. Liu, *J. Am. Chem. Soc.*, 2021, **143**, 13103–13112.
6 J. V. Kildgaard, H. A. Hansen and T. Vegge, *J. Phys. Chem. C*, 2021, **125**, 14221–14227.
7 E. Gomez, B. Yan, S. Kattel and J. G. Chen, *Nat. Rev. Chem.*, 2019, **3**, 638–649.
8 Z. Xie, E. Gomez and J. G. Chen, *AIChE J.*, 2021, **67**, e17249.
9 A. N. Biswas, Z. Xie and J. G. Chen, *Joule*, 2022, **6**, 269–273.
10 Z. Xie, E. Gomez and J. G. Chen, *AIChE J.*, 2021, **67**, e17249.
11 A. V. Milkov, S. Schwietzke, G. Allen, O. A. Sherwood and G. Etiope, *Sci. Rep.*, 2020, **10**, 4199.
12 J. H. Sinfelt, *Sci. Am.*, 1985, **253**, 90–101.
13 M. Myint, B. Yan, J. Wan, S. Zhao and J. G. Chen, *J. Catal.*, 2016, **343**, 168–177.
14 Y. Zhou, J. Lin, L. Li, M. Tian, X. Li, X. Pan, Y. Chen and X. Wang, *J. Catal.*, 2019, **377**, 438–448.
15 Y. Zhou, F. Wei, J. Lin, L. Li, X. Li, H. Qi, X. Pan, X. Liu, C. Huang, S. Lin and X. Wang, *ACS Catal.*, 2020, **10**, 7619–7629.
16 B. Yan, S. Yao, S. Kattel, Q. Wu, Z. Xie, E. Gomez, P. Liu, D. Su and J. G. Chen, *Proc. Natl. Acad. Sci. U. S. A.*, 2018, **115**, 8278–8283.
17 Z. Xie, Y. Xu, M. Xie, X. Chen, J. H. Lee, E. Stavitski, S. Kattel and J. G. Chen, *Nat. Commun.*, 2020, **11**, 1887.
18 B. Yan, X. Yang, S. Yao, J. Wan, M. Myint, E. Gomez, Z. Xie, S. Kattel, W. Xu and J. G. Chen, *ACS Catal.*, 2016, **6**, 7283–7292.
19 Z. Xie, B. Yan, J. H. Lee, Q. Wu, X. Li, B. Zhao, D. Su, L. Zhang and J. G. Chen, *Appl. Catal., B*, 2019, **245**, 376–388.
20 N. J. Escorcia, N. J. LiBretto, J. T. Miller and C. W. Li, *ACS Catal.*, 2020, **10**, 9813–9823.
21 M. Numan, E. Eom, A. Li, M. Mazur, H. W. Cha, H. C. Ham, C. Jo and S.-E. Park, *ACS Catal.*, 2021, **11**, 9221–9232.
22 T. Ma, S. Wang, M. Chen, R. V. Maligal-Ganesh, L.-L. Wang, D. D. Johnson, M. J. Kramer, W. Huang and L. Zhou, *Chem*, 2019, **5**, 1235–1247.
23 Z. Xie, D. Tian, M. Xie, S.-Z. Yang, Y. Xu, N. Rui, J. H. Lee, S. D. Senanayake, K. Li, H. Wang, S. Kattel and J. G. Chen, *Chem*, 2020, **6**, 2703–2716.
24 Z. Xie, X. Wang, X. Chen, P. Liu and J. G. Chen, *J. Am. Chem. Soc.*, 2022, **144**, 4186–4195.
25 Z. Wei, J. Sun, Y. Li, A. K. Datye and Y. Wang, *Chem. Soc. Rev.*, 2012, **41**, 7994–8008.
26 E. Gomez, S. Kattel, B. Yan, S. Yao, P. Liu and J. G. Chen, *Nat. Commun.*, 2018, **9**, 1398.
27 N. Artrith, Z. Lin and J. G. Chen, *ACS Catal.*, 2020, **10**, 9438–9444.
28 M. Chen, J. Xu, Y.-M. Liu, Y. Cao, H.-Y. He and J.-H. Zhuang, *Appl. Catal., A*, 2010, **377**, 35–41.
29 M. Chen, J. Xu, Y. Cao, H.-Y. He, K.-N. Fan and J.-H. Zhuang, *J. Catal.*, 2010, **272**, 101–108.
30 M. Chen, J.-L. Wu, Y.-M. Liu, Y. Cao, L. Guo, H.-Y. He and K.-N. Fan, *Appl. Catal., A*, 2011, **407**, 20–28.
31 J. Ye, C. Liu and Q. Ge, *J. Phys. Chem. C*, 2012, **116**, 7817–7825.
32 G. Kresse and D. Joubert, *Phys. Rev. B: Condens. Matter Mater. Phys.*, 1999, **59**, 1758–1775.
33 P. E. Blöchl, *Phys. Rev. B: Condens. Matter Mater. Phys.*, 1994, **50**, 17953–17979.

34 J. P. Perdew, K. Burke and M. Ernzerhof, *Phys. Rev. Lett.*, 1996, **77**, 3865–3868.
35 G. Kresse and J. Furthmüller, *Comput. Mater. Sci.*, 1996, **6**, 15–50.
36 Z. Xie, H. Guo, E. Huang, Z. Mao, X. Chen, P. Liu and J. G. Chen, *ACS Catal.*, 2022, **12**, 8279–8290.
37 Z. Mao, Z. Xie and J. G. Chen, *ACS Catal.*, 2021, **11**, 14575–14585.
38 E. Gomez, X. Nie, J. H. Lee, Z. Xie and J. G. Chen, *J. Am. Chem. Soc.*, 2019, **141**, 17771–17782.
39 C. Tu, H. Fan, D. Wang, N. Rui, Y. Du, S. D. Senanayake, Z. Xie, X. Nie and J. G. Chen, *Appl. Catal., B*, 2022, **304**, 120956.
40 Z. Xie, E. Gomez, D. Wang, J. Hoon Lee, T. Wang and J. G. Chen, *J. Energy Chem.*, 2022, **66**, 210–217.